Localizing aeroacoustic sources in complex geometries: A hybrid method coupling 3D microphone array and time-reversal

Yinshi Zhou, Manuel A Diaz, David Marx, Régis Marchiano, Christian Prax, Vincent Valeau

Preprint published in: Journal of Sound and Vibration, 2024.
doi: https://doi.org/10.1016/j.jsv.2024.118452

Localizing aeroacoustic sources in complex geometries: a hybrid method coupling 3D microphone array and time-reversal

Yinshi Zhou[(1)], Manuel A. Diaz[(2)], David Marx[(2)],
Régis Marchiano[(3)], Christian Prax[(2)], Vincent Valeau[(2)]

(1) Sino-European Institute of Aviation Engineering, Civil Aviation University of China, Tianjin, 300300, China (2) Institut P', CNRS - Université de Poitiers - ENSMA, Site ENSIP, Bât B17, 6 rue Marcel Doré 86022 Poitiers CEDEX, France (3) Sorbonne Université, CNRS, Institut Jean Le Rond d'Alembert, 4 place Jussieu, 75005 Paris, France

Abstract Flow-induced noise is widely encountered in engineering domains, and noise source localization is the first step to understand the generation mechanisms. A large part of aeroacoustic noise measurements is performed in wind tunnels by using microphone arrays. A widespread method to identify the noise sources based on these measurements is the beamforming technique. This relies on a Green function, which ideally accounts for source type, flow, and reflecting boundaries. This function is generally not known analytically. An alternative approach is the time-reversal technique considered here. This method consists in propagating the sound field from the microphones back to focus points interpreted as sources. The back propagation can be done numerically with an acoustic propagation solver, which replaces the Green function needed in the beamforming. To date time reversal has been used to localize sound sources with flow in two-dimensions, without considering any reflecting/diffracting boundary. The objective of this work is to consider a three-dimensional situation with flow, and to include the presence of such boundaries to see if this can improve source localization. A synthetic sound source enclosed in a streamlined body is placed in a wind tunnel, and its sound field is diffracted by a nearby airfoil. A three-dimensional antenna with 768 microphones is used to measure the sound field, and time-reversal is performed by solving the three-dimensional linearized Euler equations with a discontinuous Galerkin method. The interest of taking into account the airfoil geometry for source localization is discussed, and some comparisons with the beamforming method are performed.

Keywords: time-reversal ; beamforming ; aeroacoustic sources ; microphones ; wind tunnel

1 Introduction

Flow-induced noise is widely encountered in engineering domains such as flight and ground vehicles, submarines and wind turbines. Noise source imaging techniques allow to estimate, using microphone array measurements, the noise source distribution in terms of location, frequency, and strength. When coupled with flow measurements, they make it possible to understand the associated noise generation mechanisms and allow noise control strategies. The most common technique

is the conventional beamforming technique. A complete introduction to beamforming can be found in the references of Sijtsma [1] or Allen *et al.* [2]. Many other array processing techniques have been developed and used for aeroacoustic applications over the last decades, including for instance, beamforming deconvolution techniques (CLEAN [3], DAMAS [4]), Generalized Inverse Beamforming [5], Bayesian regularization techniques [6, 7], etc.

Acoustic imaging techniques require a propagation model. Most of the time, the analytical Green function of the propagation equation in free field is used in this purpose. However, realistic scenarios involve arbitrary flows due to real wind-tunnel operating conditions, but also possible diffraction phenomena that are due to the experimental facility (wind-tunnel elements, masts), or to the objects under study (*e.g.,* wings or blades at high frequencies [8]). In the case of open test-sections wind-tunnels, some simplified analytical models of convection-refraction through the shear layers of the flow can be used and are efficient for beamforming results [9]. In the case of closed section wind-tunnels, reflections can be accounted for in the beamforming propagation model by considering image sources [10]. On the other hand, the presence of diffracting objects in the flow is rarely taken into account, because analytic Green functions are most of the time very difficult to derive. Numerical simulation can be used in this purpose, for example by computing the time-domain Green function in order to account for the presence of diffracting objects in the flow [11]. Similar approaches can also be employed without flow [12]. To avoid computing the Green function, it is also possible to simulate numerically the wave equation and account for the boundaries in the solver, which as been done without flow in [13] and is close in spirit to the method we will present below with flow.

Over the last years, some alternative approaches for identifying aeroacoustic sources have been developed based on the time-reversal (TR) technique. This array processing technique was originally proposed by Fink *et al.* [14, 15] for solving inverse problems in complex media without flow. TR requires two steps. In the first step, the unknown source emits a sound which propagates to and is recorded by microphones. In the second step, the microphones act as sources and replay in reverse order the signals received during the first step. This operates a back propagation of the sound field. The focalization spots in this sound field are interpreted as noise sources. The theory of TR is based on two assumptions: (i) the invariance of the propagation equation by time inversion; (ii) the reciprocity property in the propagation medium. The specificity of aeroacoustic problems is the presence of flows, such as boundary layers, wakes, or shear layers in the open test section of wind-tunnels. The flow is both the source of sound and the propagation medium. An effect of the flow as a propagation medium is that it breaks the time-reversal invariance of the equations [16]. This invariance can be restored only if during the TR process the direction of the background mean flow is reversed. This flow reversal is difficult, if not impossible, to realize experimentally, especially for flows around bodies of complex geometries. Therefore, the flow direction was reversed in a numerical way for the TR process in several research studies about aeroacoustic noise source identification [17, 18, 19]. In uniform flows, flow reversal is sufficient to also ensure reciprocity. In shear flows, reciprocity is lost, but good TR results are obtained nevertheless, as shown in Rakotoarisoa [20], which explains why TR can be used in aeroacoustic source localization.

The first applications of time reversal to aeroacoustics were purely numerical. Deneuve *et al.* [17] considered the noise sources in a shear layer using the two-dimensional (2D) Euler equations. The flow variables were stored at the computational boundaries during the simulations. The time-

reversed acoustic pressure fields were reconstructed numerically, from which a sensitivity analysis based on the complex differentiation method was carried out to detect the regions of sound generation. An equivalent problem was studied by Druault *et al.* [18] for a dissipative medium, in which the TR technique allowed to detect noise sources in a turbulent flow despite the lack of reversibility. Rakotoarisoa *et al.* [19, 20] compared the TR technique and the beamforming technique with ray tracing [21] for noise source identification in heated flows.

Numerical TR can also be used to process experimental data. Padois *et al.* [22] demonstrated for the first time the possibility of using the TR technique to locate different noise sources in a low Mach number flow in an anechoic wind tunnel. The TR process was implemented numerically by solving the Linearized Euler Equations (LEE) [23] using the experimental data collected with a linear array located outside the wind-tunnel flow region. The mean flow velocity field used for the TR simulations, including the free-stream flow and the shear layers of the wind-tunnel jet, was measured beforehand. The time-reversed acoustic pressure field was reconstructed, from which the position of a monopolar noise source was estimated with an error inferior to the wavelength. Rakotoarisoa *et al.* [24] performed acoustic measurements in a wind-tunnel using a planar microphone array, and applied the TR technique (based on the LEE) to localize intermittent noise sources from a three-dimensional bluff body located in the flow. However, the solid boundaries of the body were not included. Wei *et al.* [25] proposed a method combining an analytical implementation of the TR technique with a shear layer correction, in order to estimate the time-domain sound source signals in an anechoic wind tunnel.

Recently, some studies attempted to take into account the solid boundaries of objects during the numerical TR process. Mimani *et al.* [26] conducted far-field acoustic measurements on a full-span circular cylinder using two linear arrays located on each side of a cylinder. Numerical TR was used to reconstruct the time-reversed acoustic pressure field by solving the 2D LEE, from which the dipolar nature of the Aeolian tone was revealed with a small error of 3/20 of the wavelength. This good spatial resolution during the TR process resulted both from a technique called PTRSL [27, 28] and from the modeling of the acoustic reflections on the experimental set-up. The interest of accounting further for the scattering due to solid boundaries during the TR process was demonstrated by the same authors *et al.* [29]. For a rod-airfoil pair placed in a wind tunnel, a significant improvement of the spatial resolution returned by 2D numerical TR was obtained when these solid boundaries were modelled. However, this modelling was rather crude and only one mesh point for the airfoil thickness was used, which was justified because the airfoil thickness is very small in comparison to the wavelengths of interest.

In this paper, we aim to introduce a novel approach that combines experimental measurements using a three-dimensional (3D) array with 768 microphones, and the time-reversal method with a 3D numerical solver for localizing sound sources in a wind-tunnel flow when scattering effects are very strong. To our knowledge, the 3D identification of aeroacoustic sources taking into account solid boundary effects produced by complex geometries, without simplification, has not been reported previously. The problem addressed in this paper aims to generate within the wind-tunnel flow an artificial noise source whose radiation undergoes severe diffraction and reflection effects, due to the presence of an airfoil disturbing the sound propagation from this source.

The paper is organized as follows: in Section 2, we present the anechoic wind tunnel, acoustic

source setup, and the microphone array used for our experiments. In Section 3, we summarize the 3D TR method. The numerical solvers based on the LEE for the acoustic simulation, and on the Reynolds-Averaged Navier-Stokes (RANS) equations for the simulation of the mean flow field are presented. The interpolation of the mean flow on the acoustic grid and the method for enforcing the experimental acoustic data at the boundaries of the acoustic simulation domain are discussed. We present the results for the identification of the noise sources in Sections 4 (without flow) and 5 (with flow). In section 6, we summarize our findings and provide concluding remarks on the effectiveness and implications of our proposed approach.

2 Experimental Setting

2.1 Anechoic wind tunnel

The anechoic wind-tunnel BETI at Institut Pprime is an Eiffel-type wind-tunnel with an anechoic chamber of 90 m^3 having a cutoff frequency of 200 Hz. It is built for aerodynamic and aeroacoustic studies. The test section, shown in Fig. 1, is located in the anechoic chamber between the nozzle and the collector and can be fully open or 3/4 open depending on whether a floor plate is mounted. In the present experiments, the fully open configuration is used. The wind-tunnel flow is created by a fan located downstream of the collector. This flow enters the test section through a nozzle having a contraction ratio of 10 and ending with a square section of 0.7×0.7 m^2. The maximum free-stream velocity of the wind-tunnel jet flow at the nozzle exit is 60 ms^{-1}, and the turbulence intensity is about 1.5%. The length of the test section in the flow direction is 1.44 m. At the exit of the test section the flow is collected by a collector of dimensions (width $\times$ height) 1.00×0.87 m^2. The right-handed coordinate system (O, x, y, z), also used in the numerical simulations, is depicted in Fig. 1. Its origin O is located at the center of the line AB. The x-axis is oriented in the stream-wise direction, and the z-axis in the vertical direction.

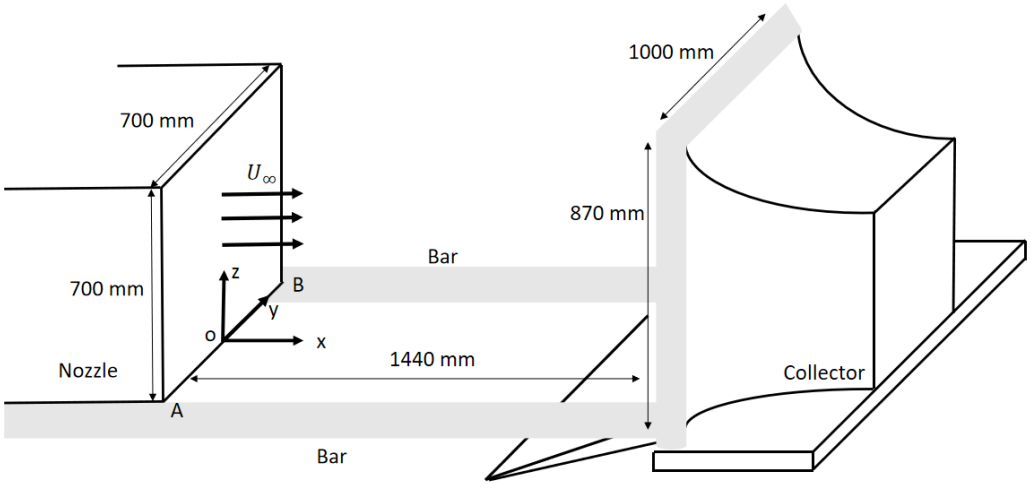

Figure 1: Sketch of the wind-tunnel BETI in the fully open configuration.

2.2 Acoustic source setup

In order to test the efficiency of the localization method in the presence of reflecting surfaces, we use a setup made of a controlled source enclosed into a streamlined body and an airfoil which reflects and diffracts the sound emitted by that source. This mimics in a basic way an installation effect. The setup is shown in Fig. 2(a). The relative positions between the nozzle of the wind tunnel, the airfoil and the streamlined body are shown by a simplified side view in Fig. 2(b). The airfoil diffracting the sound emitted by the source is a NACA 0012 airfoil with a 200 mm chord and a span of 890 mm, and its leading edge is located at a distance of 310 mm from the nozzle exit plane. The airfoil is held by two beams placed outside of the flow and passes entirely through the open test section in the vertical direction. The upstream nose of the streamlined body is located at a distance of 181 mm from the nozzle exit plane.

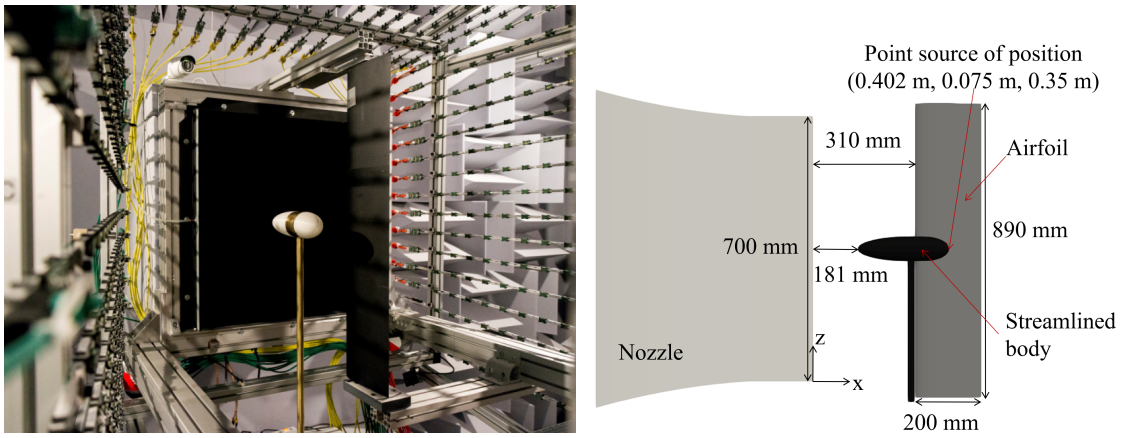

(a) (b)

Figure 2: (a) The streamlined acoustic source besides a NACA 0012 airfoil with a finite span in the open test section of the wind-tunnel; (b) sketch of the streamlined body, airfoil and the nozzle of the wind tunnel.

Fig. 3(a) shows the structure and the dimensions of the streamlined acoustic source. The shape of the streamlined body is designed to minimize the flow perturbation and potential aeroacoustic noise emissions. A compression chamber embedded inside this body generates sound that propagates through a conical tube and is radiated outside through an orifice of diameter 5 mm located at the downstream extremity of the object. The center of this orifice, located at position (0.402 m, -0.075 m, 0.35 m), is considered as the known source position. A metallic cylinder with a diameter of 20 mm is used as support, as can be seen in Fig. 2(a), and the translation of the streamlined acoustic source in the $x-$direction and $y-$direction is controlled by a robotic system. Fig. 3(b) shows the far-field acoustic spectrum of the streamlined source for the experimental configuration described above, which was measured by a measurement microphone (a G.R.A.S Type 40AF model with the preamplifier being 01dB-Stell Type PRE21S/PRE21A) placed in position (0.544 m, -0.662 m, 0.365 m), with a distance of about 0.6 m from the source position.

The frequency peaks in the spectrum originate from the resonances of the tube connecting the compression chamber to the outlet orifice. Additionally, the emission level is sufficient for

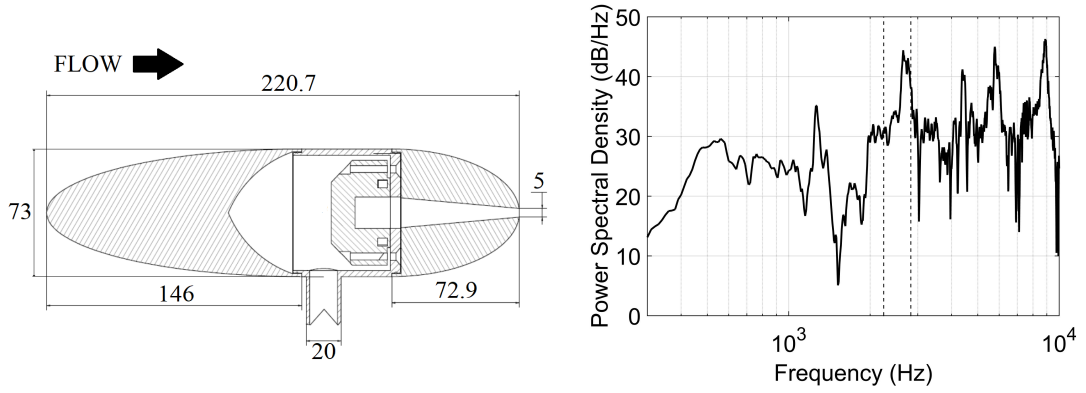

(a) (b)

Figure 3: (a) The structure and the dimensions (in mm) of the streamlined acoustic source; (b) Far-field acoustic power spectral density for the broadband streamlined acoustic source. The frequency band between the dashed lines indicates the third-octave band [2245 Hz; 2828 Hz].

measurements of frequencies higher than 2 kHz thanks to the characteristics of the compression chamber. In the following, the third-octave band [2245 Hz; 2828 Hz] will be processed.

2.3 Microphone array

The acoustic data are generated by using a 3D microphone array designed at Institut Jean le Rond d'Alembert (the MegaMicros system [30]) and forming a tunnel of 1024 digital MEMS microphones around the flow under study [31]. The data acquisition system is not a commercial product, it is homemade. The 1024 MEMS microphones are divided into 128 bundles, each containing 8 microphones. Each microphone is integrated into a small PCB card (see Fig. 2(a)). Within each bundle, the 8 microphones are controlled by a buffer card connected to the data acquisition system via an RJ45 cable (colored cables on Fig. 4(b)). From the MEMS microphones to the acquisition system interface, signals are handled with the I2S serial protocol. Then signals are multiplexed and transferred via a USB 3.0 serial bus to the host PC, further details can be found in [31]. The sampling rate is 50 kHz in this study. Fig. 4(a) shows the 3D model of the array structure, *i.e.,* a cone with square bases, which enlarges from the nozzle to the collector of the wind-tunnel.

This type of design allows to account for the development of the shear layers from the nozzle and to avoid the turbulent regions around the collector. More specifically, the distance between square base 1 (vertices 1, 2, 3 and 4) and square base 2 (vertices 5, 6, 7 and 8) is 1157 mm with their edge length being respectively 1200 mm and 1535 mm. This structure thus contains four plane surfaces (denoted by 'left', 'top', 'right' and 'bottom'), each having 16 bars, spaced by a distance of 75 mm on square base 1 and 96 mm on square base 2. Each bar has a U-shaped section with a length of 1.8 m, which allows to mount 16 microphones on them, spaced uniformly with a gap of 72 mm between two neighbouring microphones. Note that the supports of the test models cross the side 'bottom' of the array structure. Therefore, only 3 sides ('left', 'top' and 'right') with 768 microphones, enclosing the open test section of the wind tunnel, are used for the experiments in this paper. With the consideration of the mechanical and mounting constraints, the chosen arrangement

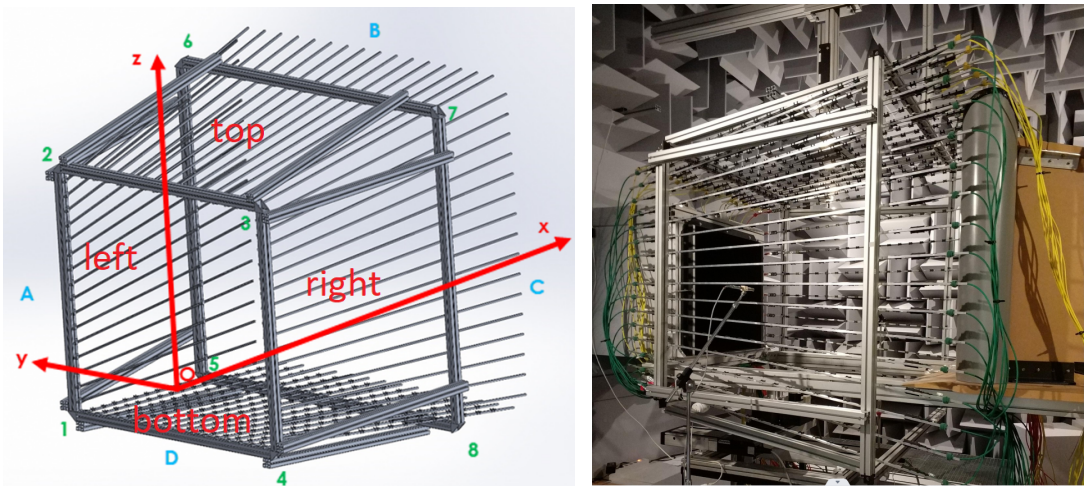

(a) (b)

Figure 4: (a) 3D model of the array structure [31]; (b) photography showing the wind-tunnel components with the installed microphone array. From left to the right are respectively the nozzle, the microphone array and the collector.

of microphones is optimized among several options in terms of frequency resolution and relative levels between main and side lobes given by the beamforming technique [31]. Fig. 4(b) shows the microphone array installed in the test section of the wind-tunnel.

The microphone relative positions are well known because of the rigid structure of the array. Nevertheless, a geometrical calibration of the array was carried out based on the process proposed by Vanwynsberghe *et al.* [32]. More details of the calibration of the array are described in [31]. By subtracting to the relative coordinates the position errors in x, y and $z-$directions, the absolute coordinates of the 768 microphones were then obtained.

3 Hybrid digital/experimental 3D Time Reversal for aeroacoustics

3.1 3D Time Reversal for aeroacoustics

3.1.1 Model for the propagation of acoustic waves: the linearized Euler equations

The propagation of acoustic perturbations in three spatial dimensions (3D) within an inhomogeneous mean flow can be modeled using the linearized Euler equations (LEE) [33]. In primitive variables, the 3D LEE model is represented as:

$$\boldsymbol{q}_t + \boldsymbol{E}_x + \boldsymbol{F}_y + \boldsymbol{G}_z + \boldsymbol{M}_0\boldsymbol{q} = \boldsymbol{0} \tag{1}$$

Here, $\boldsymbol{x} : x, y, z \in \Omega$ and $t \geq 0$, while $\boldsymbol{q}(\boldsymbol{x}, t)$ represents the vector of evolved quantities, and $\boldsymbol{E}$, $\boldsymbol{F}$, and $\boldsymbol{G}$ are the associated fluxes for each Cartesian direction. The operator $\boldsymbol{M}_0$ accounts for

medium inhomogeneities. The evolved quantities are defined as $\boldsymbol{q} = (\rho_a, u_a, v_a, w_a, p_a)^\intercal$, where the quantities represent the perturbations in density, acoustic velocity in the three spatial dimensions, and pressure, respectively. The flux terms can then be expressed as follows:

$$\boldsymbol{E}(\boldsymbol{q}) = \begin{bmatrix} \varrho_a u_0 + \varrho_0 u_a \\ u_0 u_a + p_a \varrho_0^{-1} \\ u_0 v_a \\ u_0 w_a \\ u_0 p_a + \gamma p_0 u_a \end{bmatrix}, \; \boldsymbol{F}(\boldsymbol{q}) = \begin{bmatrix} \varrho_a v_0 + \varrho_0 v_a \\ v_0 u_a \\ v_0 v_a + p_a \varrho_0^{-1} \\ v_0 w_a \\ v_0 p_a + \gamma p_0 v_a \end{bmatrix}, \; \boldsymbol{G}(\boldsymbol{q}) = \begin{bmatrix} \varrho_a v_0 + \varrho_0 v_a \\ w_0 u_a \\ w_0 v_a \\ w_0 w_a + p_a \varrho_0^{-1} \\ w_0 p_a + \gamma p_0 w_a \end{bmatrix}, \tag{2}$$

while the product $\boldsymbol{M}_0\boldsymbol{q}$ reads:

$$\boldsymbol{M}_0\boldsymbol{q} = \begin{bmatrix} 0 \\ -u_a \left(\frac{\partial v_0}{\partial y} + \frac{\partial w_0}{\partial z} \right) + v_a \frac{\partial u_0}{\partial y} + v_a \frac{\partial u_0}{\partial z} + \left(p_a \frac{\partial \varrho_0}{\partial x} - \varrho_a \frac{\partial p_0}{\partial x} \right) \varrho_0^{-2} \\ u_a \frac{\partial v_0}{\partial x} - v_a \left(\frac{\partial u_0}{\partial x} + \frac{\partial w_0}{\partial z} \right) + w_a \frac{\partial v_0}{\partial z} + \left(p_a \frac{\partial \varrho_0}{\partial y} - \varrho_a \frac{\partial p_0}{\partial y} \right) \varrho_0^{-2} \\ u_a \frac{\partial w_0}{\partial x} + v_a \frac{\partial w_0}{\partial y} - w_a \left(\frac{\partial u_0}{\partial x} + \frac{\partial v_0}{\partial y} \right) + \left(p_a \frac{\partial \varrho_0}{\partial z} - \varrho_a \frac{\partial p_0}{\partial z} \right) \varrho_0^{-2} \\ (1-\gamma) \left(p_a \left(\frac{\partial u_0}{\partial x} + \frac{\partial v_0}{\partial y} + \frac{\partial w_0}{\partial z} \right) - u_a \frac{\partial p_0}{\partial x} - v_a \frac{\partial p_0}{\partial y} - w_a \frac{\partial p_0}{\partial z} \right) \end{bmatrix}. \tag{3}$$

Here, $\gamma = 1.4$ is the ratio of heat capacities, and $\varrho_0, u_0, v_0, w_0, p_0$ represent the mean flow properties: density, flow velocity in the three spatial dimensions, and pressure, respectively.

3.1.2 3D Time Reversal in aeroacoustics

The linearized Euler equations are invariant under the following change of variables:

$$\begin{cases} t \to -t, \\ \rho_a(\mathbf{x}, t) \to \rho_a(\mathbf{x}, -t), \\ \mathbf{v_a}(\mathbf{x}, t) \to -\mathbf{v_a}(\mathbf{x}, -t), \\ p_a(\mathbf{x}, t) \to p_a(\mathbf{x}, -t), \end{cases} \tag{4}$$

The first line represents the classical time reversal in acoustics [14, 34]. In scenarios involving waves without flow, the time reversal method consists of recording the acoustic wavefield at a set of receivers, reversing the time axis of the recorded signals, and re-emitting them back into the medium. This causes the waves to propagate backward and focus at the original source location. However, when flows are present, this change alone is not sufficient; it is also necessary to change the sign of the velocity fields within the flow to ensure the invariance of the equations [17, 22, 20]. From a numerical perspective, this operation is straightforward and is realized by the sign inversion of the velocity in the third line of Eq. (4).

3.2 Numerical solvers

3.2.1 Numerical solver for the propagation of acoustic waves

The LEE equations are numerically solved using the nodal discontinuous Galerkin method [35]. The equations are discretized over a set of elements within an unstructured mesh, enabling the acoustic field of each element, $\boldsymbol{q}^k$, to be represented using high-order polynomial base functions. The mesh consists of volumetric elements (Fig.5(a)) within the 3D domain and surface elements (Fig.5(b)) on the boundaries of the 3D domain. Employing an unstructured mesh is essential for incorporating complex objects, such as airfoils or streamlined sources, into the computational domain.

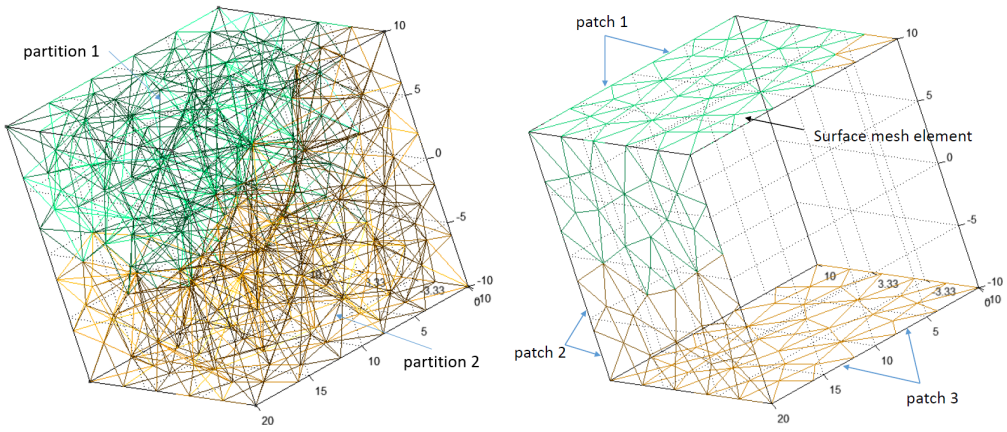

(a) (b)

Figure 5: A 3D mesh with two partitions for a cubic domain: (a) volume mesh; (b) surface mesh.

The mesh can be divided into several partitions (indicated by different colors in Fig. 5) to enable parallel computation, where each partition is computed by one processor. For the initial conditions, we assume an unperturbed field: $\boldsymbol{q}(\boldsymbol{x}, t) = 0$. Various boundary conditions are employed: rigid wall with slip condition (noted "wall" thereafter) at the boundary of objects or at the bottom of the domain [36], transparent conditions on inlet and outlet boundaries [36], and active boundaries on the sides where the reversed signal from the microphones is injected (see the subsequent section for details on this aspect).

3.2.2 Simulation of the base flow with a RANS simulation

The TR technique used for noise source identification in a flow with the presence of solid boundaries is conducted with the LEE and requires the mean flow information around the objects in the whole portion of the wind tunnel included in the computational domain of the LEE simulations. Measuring this flow experimentally would be extremely cumbersome. Hence, the strategy here is to compute the mean flow in the wind tunnel by solving the Reynolds-Averaged Navier-Stokes (RANS) equations to limit the computational cost. This is conducted by using the open source CFD solver OpenFOAM. This includes a RANS solver with different turbulence models, and a $k-\omega$ SST model is employed. Among different turbulence models [37], Menter [38] concluded that this model allows to accurately predict pressure-induced separation and is a good choice for aerodynamic applications. In this paper *simpleFoam*, the OpenFoam solver based on the SIMPLE algorithm for incompressible turbulent flow, is used for the RANS simulation, and first- and second-order schemes were implemented to discretize the convective terms. A first-order upwind discretization in space was first used to avoid divergence of numerical simulation, the results of which served as the initial assumption for the second-order method. A second-order linear upwind method was then used for the discretization to obtain results with higher accuracy. A residual level of 10^{-8} was used for the convergence of pressure, velocity and turbulence quantities. For the 3D mesh in the RANS simulations, which has to include the airfoil sharp trailing edge and the streamlined body, the mesh generator of Star-CCM+ has been used. The mesh and the mean flow will be presented in Section 5.1. For the computation in that section, a parallel simulation using 80 processors is

performed. Once computed, the mean flow information serves as input data for the TR technique for the cases with background flow.

3.3 Coupling between experimental and numerical data

The implementation of 3D TR requires an interpolation of the based flow on the acoustic grid. An open source software GMSH was used for acoustic mesh generation with tetrahedron elements, in which nodes are also added. The CFD mesh contains basically hexahedron elements. The mean flow information should be mapped to the grids of acoustic mesh. This interpolation process is achieved using a function of MATLAB.

3.4 Injection of the time reversed microphones data on the boundaries of the numerical domain

As explained previously, the first step involves recording signals from the microphone array. To apply the time reversal method, these signals are time-reversed and used as an active boundary in the 3D numerical solver solving the LEE. Two stages are required for this process. First, all the signals must be resampled at the sampling frequency of the numerical simulation, which is higher than the experimental one. Second, the signals need to be used as boundary conditions in the 3D numerical solver, and three approaches were considered:

(i) using the nodes closest to the microphones to introduce the channels of signals,

(ii) interpolating these signals to the closest nodes to the microphones,

(iii) injecting the signals on Gaussian patches,

The former two strategies proved to be numerically impractical; the first one is not accurate, while the second one requires significant computational resources. Therefore, to properly introduce the channels of signals at a set of isolated positions, we choose to use the Gaussian patches injection.

To impose this kind of boundary condition, the following field is prescribed on the faces of the elements coinciding with the panels of the microphone antenna:

$$\boldsymbol{q}^{\boldsymbol{R}}(\boldsymbol{x}, n\Delta t) = \sum_{j=1}^{N_{mic}} (0,0,0,0,f_j^n)^{\intercal} \exp\left(-\frac{(\boldsymbol{x}-\boldsymbol{x}_j)^2}{\sigma^2}\right) \tag{5}$$

where $\boldsymbol{q}^{\boldsymbol{R}}$ represents the solution on the outer face of a tetrahedral element. This vector is used to reconstruct the numerical flux at the boundary of the element computed here using the Lax-Friedrichs method [35]. This allows imposing only the incoming waves and allows outgoing waves originating from within the domain to exit.

The parameter f_j^n is the amplitude of the time reversed pressure signal at the n-th time step for the j-th channel. The parameter σ is a free parameter used to control the spatial size of the Gaussian function, its size should be chosen to avoid overlapping with any neighboring sensor, ensuring that the function remains compact on the boundary for introducing each j-th channel individually. To this end, the value of σ is set as 0.03 m in this paper. This strategy has proven suitable for introducing the multiple channel signals. Therefore, we will refer to it as the "Gaussian spots" boundary.

4 Results without flow

In this section, the objective is to see if accounting for the diffracting body in the source localization process can be beneficial. Flow is not crucial in this regard and measurements are thus performed without flow. We first discuss the computational domain for the time reversal and provide some details about the practical implementation. Then we perform localization by ignoring the presence of the diffracting body, which allows a comparison of TR and beamforming. Finally we include the presence of the diffracting body during the TR to see if this can improve the localization.

4.1 3D numerical TR without flow implementation

Figure 6(a) shows the geometry of a NACA 0012 airfoil at an angle of attack of 0° and the streamlined acoustic source. In this figure, only 256 microphones are shown for clarity, they form a subset of the 768 microphones of the full array shown in Fig. 6(b). In the following, either all 768 available microphones, or the subset of 256 microphones will be used for our processing. Using the coordinate system described in section 2.1, the synthetic noise source is located at the center of the orifice of the streamlined body, that is at position (0.402 m, -0.075 m, 0.35 m). The leading edge of the airfoil is located at a distance of 310 mm from the patch 'Front' corresponding to the nozzle exit (see also Fig. 2(b)). To conduct parallel computation, the unstructured 3D acoustic mesh is divided into 200 partitions. Some refinements around the surfaces of the airfoil and the streamlined acoustic source are generated in order to well describe the geometry for the 3D TR simulation. The 3D acoustic mesh contains 1839344 elements including 1733448 tetrahedra inside the domain of 3D acoustic mesh and 105896 triangles on all the patches of the boundary of the domain. Figure 6(c) shows the triangular mesh elements on the patches of 'Airfoil' and 'StreamlinedSource' using the "`wall`" boundary condition. Figure 6(d) shows the triangular mesh elements on the patches of 'Left', 'Top', and 'Right'. For the 3D TR simulations, the size of these elements is well defined in order to allow the Gaussian spots at each position of microphones to contain enough mesh grids. First of all, the acoustic signals are filtered by a band-pass filter of 256^{th} order to conduct TR simulations in the third-octave band [2245 Hz; 2828 Hz]. Then interpolations in time should be conducted for the experimental data in order to be applied to the 3D TR process for the reason that the time step for the numerical simulation (which depends on the CFL number, the mesh element size, the background flow field and the the polynomial order N) is much smaller than the sampling period is $2{\times}10^{-5}$ s of the experimental data. For 3D TR simulations without flow with the consideration of solid boundaries, the time step for the numerical simulation is 1.77×10^{-7} s. The physical simulation time for the 3D TR is 0.02 s with the polynomial order $N = 2$. Therefore, 1002 data points were used for the interpolation process. Fig. 7 shows the original signal of the microphone 545 and the corresponding signal after interpolations.

4.2 Beamforming and TR results without considering solid boundaries

In this section, the synthetic noise source is localized by ignoring the presence of solid boundaries. In addition to TR, the beamforming is used as a benchmark method. 256 channels of data were selected from the acoustic measurement database by the microphone array of 768 microphones. The positions of the corresponding microphones are shown in Fig. 6(a). Acoustic data from the 256 channels were recorded at a sampling frequency of 50 kHz with a sampling time of 10 s. The implementation of the 3D beamforming associated with the deconvolution method CLEAN-SC allows to identify noise sources in a 3D volume with good spatial resolution. A 3D scanning grid

with a spatial resolution of 5 mm was set. The safety factor of the CLEAN-SC method was chosen as 0.99 and the clean beamwidth was set to 0.05 m [3]. For the array signal processing, a 256th order numerical high-pass filter with a cutoff frequency of 20 Hz was used to filter the signal of each channel. In addition, the monopolar steering vector and a free-field Green function are used for the beamforming algorithm. The airfoil effect is not taken into account for beamforming results. More details of the beamforming implementation can be found in Section 4.1 of [39]. The computation time is about four days using MATLAB on a personal computer with a 3 GHz Intel Xeon processor.

Fig. 8(a) presents the 3D sound map obtained with BF without deconvolution. The known position of the synthetic noise source (0.402 m, -0.075 m, 0.35 m) is indicated by the red cross. The sound map yields some ambiguities because of the influence of the solid boundaries of the airfoil. There is a main lobe centered on the position of the noise source together with an isolated side lobe and an ambiguous elongated side lobe. The elongated side lobe is evenly distributed along the $y-$direction and part of it is located on the side of the airfoil opposite the source. The peak level of the sound map is located at position (0.425 m, -0.095 m, 0.35 m). The CLEAN-SC technique is used in order to improve the spatial resolution of the sound map and the result is shown in Fig. 8(b), which shows that the side lobes are successfully removed. This is the case because the elongated lobe is coherent with the main lobe. A single noise source is now identified with an unchanged position at (0.425 m, -0.095 m, 0.35 m). The localization errors of the identified noise source in the $y-$direction and $x-$direction are thus respectively 0.02 m and 0.023 m, which means a localization error inferior to the wavelength.

The TR method is then used to identify the same synthetic noise source. The same experimental data of 256 channels are used for 3D TR simulation. However, microphone signals during only 0.02s are used as the input for TR simulation in order to reduce the computational cost. Typically, the simulation using 200 processors then requires about 2 days. Fig. 9(a) shows a snapshot of the pressure field in a planar cross section XY at $z = 0.35$ m when the waves inside the simulation domain reach the permanent regime. Some lobes with opposite phases in the y-direction are clearly observed. However, no dominant lobe is centered on the position of the synthetic noise source, which makes it difficult to localize the source in this representation. To identify the noise source, the RMS of the pressure field is computed. Fig. 9(b) shows the distribution of the RMS of the pressure field integrated from 0.005 s to 0.015 s in the same plane. A dominant focusing spot is found just below the known position of the noise source. The position of the identified noise source is (0.429 m, -0.105 m, 0.351 m). The identified position error is 3 cm in the $y-$direction. In addition, the TR result shows some ambiguities due to the presence of some other focusing spots the y-direction. Interestingly, this demonstrates some similarities of the TR and beamforming methods for synthetic noise source identification when solid boundaries of objects are not considered during TR simulations.

When performing TR, it may be anticipated that neglecting the diffracting body could have less impact on source localization at low frequency since the sound wavelength becomes large compared to the body size. To verify this idea, 3D TR localization of the synthetic noise source has been performed for four different frequency bands, using 768 channels of the acoustic data. Figure 10 shows, for each of these bands, the distribution of the RMS pressure field obtained by TR, integrated from 0.005 s to 0.015 s in a planar cross section XY located at $z = 0.35$ m. The lowest third-octave frequency band considered, [561; 707] Hz, for which the center frequency corresponds to a wavelength more than twice the airfoil chord, is shown in Fig. 10(a). A focalization spot is found close to the known synthetic source position indicated by a black cross, and two side-lobes of equal

amplitudes are located along the y-direction. The overall pattern is similar to what would be obtained for the detection of a monopole in free field. Similar observation is found in the third-octave band [1122; 1414] Hz in Fig. 10(b) but one notices that the top side lobe becomes larger in amplitude than the bottom one. As the frequency increases further, the side lobe in the positive y-direction becomes stronger and tends to merge with the main lobe (Fig 10(c) and Fig 10(d)). Hence, it appears that the focalization map resembles less and less that of a free field pattern as the frequency increases, emphasizing the need for accounting for the geometry at high frequency, which will be done in the next section. For the four cases, the localization errors with respect to the wavelength are respectively 12.2%, 12.2%, 37.9% and 23.0% from low- to high-frequency band. All the errors are less than half-a-wavelength. Although the third-octave band [1414; 1782] has a relative error higher than that of the third-octave band [2245; 2828] Hz, the overall trend is an increase of the relative localization error as frequency increases, as anticipated.

4.3 TR results with consideration of solid boundaries and effects of number of microphones

In the previous section, the synthetic noise source is not perfectly localized without the consideration of solid boundaries of objects for the beamforming and TR methods, and this seems to be more so at high frequency . In this section the solid boundaries of objects are modeled for 3D TR simulations, which is the main concern of this paper. In order to study the effect of the number of microphones on the TR results, two experimental configurations are considered for 3D TR simulations: one is conducted with 256 microphones, the same as for BF and TR in the previous section, the other with 768 microphones. The numerical simulations are performed in parallel on a cluster with 200 processors.

Fig. 11(a) shows the RMS of the pressure field obtained with 256 microphones. This results from an integration from 0.005 s to 0.015 s in a planar cross section XY at $z = 0.35$ m, and the focusing spot allows identifying the position of the noise source with a precision of wavelength. More specifically, the position of the identified noise source is (0.401 m, -0.080 m, 0.349 m), which represents a localization error smaller than for the case without the consideration of solid boundaries. In Fig. 11(b), the synthetic noise source is identified with the same precision in a vertical cross section XZ. In addition, two ambiguous side lobes are observed in the $z-$direction besides the focusing spot. This may due to the fact that the waves are not well established using only 256 channels of data as input data for the TR simulation. The ambiguities are much clearly shown in a cross section YZ in Fig. 11(c). The other isolated spots are located on the source sides. Interestingly, it is similar to the aliasing effects of the conventional beamforming method, which may occur when the distance between neighbouring microphones are larger than the 1/2 wavelength of the sound wave under investigation. The dominant focusing spot also reveals the identified position of the noise source (see Fig. 11(c)).

Hence, by including the solid boundaries in the 3D TR technique, and without conducting post-processing process similar to deconvolution methods, the noise source is identified with a localization error inferior to the wavelength by 3D TR. In addition, the position error in the $y-$direction is smaller than that of the BF result if we consider the peak level of the RMS of the pressure field as the identified position of the noise source. However, the 3D TR is more complex and computationally expensive compared to the beamforming method.

For TR using 768 microphones rather than the subset of 256 microphones, the position of the identified noise source is found to be (0.401 m, -0.080 m, 0.349 m), which is exactly the same as that obtained using only 256 microphones. In this case, neither a clear improvement of the resolution nor a better position localization is observed in the RMS of the pressure fields. This is observed by comparing Figs. 12(a), 12(b) and 12(c) obtained for 768 microphones to Figs. 11(a), 11(b) and 11(c) obtained for 256 microphones. However, the ambiguities (ghost images) observed in Figs. 11(b) and 11(c) are disappeared in Figs. 12(b) and 12(c), which means that there is still an advantage in using a larger number of microphones.

4.4 Use of 2D sub-antennas

Until now, only a 3D antenna has been used either for beamforming or TR, with all (768) or a restricted number (256) of microphones. To assess the benefit of using a 3D antenna rather than a more conventional planar antenna, we now perform TR localization using the microphone signals of 2D sub-antennas, namely, the sub-antennas called 'left' and 'right' in Figs. 4(a) and 6(a). The left antenna is located on the side of the airfoil opposite the streamlined source, so that the airfoil is hiding the source. The right antenna is on the same side as the source. The solid boundaries (airfoil, streamlined source) are included in the simulations. Figure 13 present results in the frequency band [2245; 2828] Hz. For the 3D TR localization with the left sub-antenna (Figure 13(a)), it is observed that the source is not localized at all due to the screening effect by the airfoil. The time-reversed acoustic field is mostly reflected by the airfoil and does not go around it. For the right sub-antenna (Fig. 13(b)) the localization is much better since the antenna has a direct view on the source. However, the best localization is returned by the full antenna (left+right+top), as seen in Fig. 11(a) when the full antenna has 256 microphones in total or in Fig. 12(a) when it has 768 microphones. This shows the advantage of using a 3D antenna surrounding the bodies, in particular when screening effects are present. In order to see if the situation can be modified at lower frequency when the sound gets less diffracted by the airfoil, localization with 2D sub-antennas is performed in the lower frequency band [561; 707] Hz, and the result is shown in Fig. 14. The observations and conclusions are mostly unaffected.

5 Results with flow

In this section, we present the result of acoustic source localization in the presence of flow. As the flow needs to be accounted for during the TR numerical step, it needs to be known. We thus first present the computation of the mean flow using a RANS simulation, and compare it with some point measurements in the wind tunnel. Then, we present the result of TR-based source localization.

5.1 Computation of the mean flow

In order to obtain the flow field around the airfoil and the streamlined body, including the shear layer developed from the outlet of the wind-tunnel, a parallel RANS simulation has been conducted (see Section 3.2.2). Figure 15(a) shows the cuboid computational domain including the nozzle, the streamlined acoustic source, the airfoil, and the collector. The dimension of the cuboid domain is 3.99 m $\times$ 6.40 m $\times$ 3.26 m. Some geometrical elements like the bars, the support of the testing

models, and the microphone array are not accounted for, as they are not suspected to affect importantly the mean flow. Fig. 15(b) shows a planar cross section XY of the mesh at $z = 0.35$ m, which clearly indicates the refinement zones corresponding to the shear layer and wakes of the testing models. All tunnel walls and the solid boundaries of the testing objects were computed with a non-slip boundary condition, so boundary layer mesh need to be generated on the corresponding patches of the computational domain. The values of $y+$ related to the first layer grid near the wall is checked for the results of RANS simulations, which are less than 30 required by the wall function used for the numerical simulations. The RANS simulation requires some boundaries conditions for the pressure, velocity and turbulence intensity for different patches of the geometry. Most of them are standard and we concentrate on the inflow velocity boundary condition at the nozzle exit. This should be defined so that it leads to the same shear layer development as in the actual wind tunnel. An analytical velocity profile is used, in which the parameters are determined by measurements. The profile is the one proposed by Candel [40]:

$$\frac{U}{U_0} = \frac{1}{2}(1 - \tanh(\eta_{cm})), \tag{6}$$

where U_0 is the jet velocity of the incoming flow. The normalized coordinate η_{cm} is given by the following equation

$$\eta_{cm} = \frac{2(z - z_{cm})}{\delta_{cm}}, \tag{7}$$

where z_{cm} is the position of the inflection point of the shear layers and δ_{cm} is the half thickness of the shear layer. The analytical velocity profile is shown in Fig. 16(a) with the inflection point of the shear layers indicated by a circle symbol. The thickness of the shear layer is estimated based on flow measurements made in the wind-tunnel in the wake of one of the nozzle four walls, using a hot-wire anemometer without any objects in the test section of the wind-tunnel. Its value is set at $\delta_{cm} = 0.0217$ m at $x = 0$ m in order to implement the velocity boundary condition for numerical simulations. This 1D velocity profile needs to be transformed into a whole 2D velocity profile in the nozzle exit plane. To do this, the exit plane is divided into four parts (A, B, C and D) as shown in Fig. 16(b), and in each of those the analytical solution of Eq. (7) is adapted and applied.

Fig. 17(a) shows an overview of the computed mean axial velocity field for a cross section XY located at $z = 0.35$ m. Several features of the flow are visible, such as the shear layer developing from the outlet of the nozzle with an increasing thickness, and the wakes of the airfoil and the streamlined body. In order to verify the relevance of the computed mean flow, it is compared with the experimental data measured in the wind-tunnel with a hot-wire anemometer. The computed velocity profile is considered along a line in the $z-$direction, which starts from the point (0.15, 0, 0.65) to the point (0.15, 0, 0.75) and crosses the upper shear layer developing from the nozzle. It is compared with the corresponding experimental data in Fig. 17(b). The two velocity profiles do not collapse but are very similar, with an error less than 5%. The experimental data correspond to a situation when there is no object (airfoil) in the wind tunnel. This may explain a part of the difference, since the velocity at the nozzle decreases slightly in the presense of testing objects. It was found in the thesis of Padois [41] that the TR simulation is not very sensitive to the shear layer velocity profile. Therefore, the computed mean flow is good enough to be used as input data for 3D TR simulations in our case.

5.2 3D numerical TR with flow implementation

The background mean flow for 3D numerical TR simulations contains large velocity gradients in the shear layer, the wake of the airfoil, and the wake of the streamlined acoustic source. Therefore, the 3D acoustic mesh should also be refined in these areas in order to well present the mean flow after interpolation. To this end, some refined points are defined in order to create some mesh refinements at the points for the domain of the 3D acoustic mesh including the testing objects. In this case, 768 channels of acoustic data are used for 3D TR simulations. The arrangement of the microphones is shown in Fig. 6(b). The 3D acoustic mesh contains 4091240 elements including 3976782 tetrahedra inside the domain of 3D acoustic mesh and 105896 triangles on all the patches of the boundary of the domain. The refinements of the mesh are shown in the corresponding areas. The mean flow information serves as input data for 3D TR simulation, for which it is interpolated to the 3D acoustic mesh. The direction of the mean flow is reversed for the 3D TR process to maintain invariance of the equations by time reversal. The 768 channels of experimental data are imposed at the boundaries of the simulation domain, each of which has a Gaussian distribution in space covering enough grid points.

5.3 TR results with flow

The treatment of the experimental data including interpolation and filtering is conducted in the same way as that in section 4.1. The physical simulation time for the 3D TR is 0.02 s with the polynomial order $N = 2$. The 3D TR simulations are conducted in a cluster using 400 processors. Fig. 18 shows the 3D TR simulation result for the identification of the synthetic noise source in an incoming flow of 39.2 m/s. Fig. 18(a) shows the RMS of the pressure field from 0.005 s to 0.01 s in a planar cross section XY at $z = 0.35$ m. The position of the synthetic noise source is indicated by a black cross. It is found that a focalisation spot is centered on the black cross. Thus, the noise source position is identified by the 3D TR result. The position of the identified noise source is (0.401 m, -0.080 m, 0.352 m). The localization precision is within half-a-wavelength. In addition, several spots with lower intensity are observed beside the focalisation spot in the $y-$direction, one of which is on the surface of the airfoil. This is also clearly observed in Fig. 18(c) showing the RMS of the pressure field from 0.005 s to 0.01 s in a planar cross section YZ at $x = 0.402$ m. In Fig. 18(b), no ambiguities spots are observed thanks to the use of 768 channels of experimental data. Hence, the effects of solid boundaries of objects and the wind-tunnel flow on the noise source identification are well accounted for by the 3D TR simulation. However, the 3D TR results still presents some spots with lower intensity, which is quite similar to the side lobes of conventional beamforming results. Therefore, some post-processing treatments could be applied to the TR results in order improve the spatial resolution similar to the deconvolution methods associated to conventional beamforming. Note that the maps in Fig. 18 with flow are not very different from the ones without flow shown in Fig. 12. In particular, there appears to be little noise generated by the flow at the trailing edge of the airfoil. Measurements of the sound pressure level in the far field done with the streamlined source switched on or off (not shown) confirm that in the frequency band considered here, [2245; 2828] Hz, the noise generated by the streamlined source is dominant.

6 Conclusion

This paper has presented the application of time reversal to acoustic source localization in an aeroacoustic context. The method involves two stages. During the first and experimental stage, the sound emitted by a source placed in a wind tunnel is measured using a 3D antenna of 768 MEMS microphones. Since the objective is here to assess the whole method, the sound source is a synthetic one enclosed in a streamlined body. The streamlined body is placed next to an airfoil, the effect of which is to diffract the sound. This setup is relevant to assess whether accounting for body diffraction on the localization process is useful and realizable in practice. The second stage is performed numerically using time-reversal. During this stage, the microphone signals recorded during the first stage act as sound sources and the resulting acoustic field is computed using the linearized Euler equations. The sound then back-propagates toward the source, and focal points, associated with large root-mean-square acoustic pressure, determine the position of the acoustic sources. The numerical solver for acoustic propagation needs to match the experimental setup. Therefore, a 3D Discontinuous-Galerkin solver is used to allow for body fitted mesh, which makes it possible to include the diffracting body in the simulation. To our knowledge, this is a first application of time-reversal to sound source localization in 3D including flow and diffracting bodies.
The method has first been applied in the absence of wind-tunnel flow. In the first place, the diffracting airfoil presence was neglected during the localization process, which allowed a comparison with the classical beamforming technique. Both the TR and beamforming methods localized correctly the source. However, spurious secondary lobes are present that cross the body's position and may be interpreted partly as ghost images. For beamforming they can be removed using deconvolution techniques, but this is not the case for TR. In more complex situations, these ghost images would make the sound map more difficult to interpret. Including the diffracting airfoil in the TR simulation was shown to remove these ghost images, demonstrating the effectiveness of including diffracting bodies in the simulation domain.
The method has then been applied in the presence of wind-tunnel flow, which complicates the situation in general. Using beamforming, the Green's function would have to be known and would be approximated in practice. Using TR, the flow is automatically accounted for. However, since this is conducted numerically, the mean flow needs to be known. It is difficult to fully measure the flow, and in the present case it is obtained from a RANS simulation of the wind tunnel. With this flow and diffracting body both included in the simulation, the source was correctly localized.
This paper demonstrates the feasibility and usefulness of numerical 3D time-reversal including both the flow and sound diffracting bodies. An inconvenient of the method is its associated large computational cost.

Acknowledgements

This work is supported by Agence Nationale de la Recherche (ANR), the CPER FEDER project of Région Nouvelle Aquitaine, the Fundamental Research Funds for the Central Universities (Grant no. 210522003126) and the China Scholarship Council. The authors wish to thank Pascal Biais, Dominique Busquet, Pascal Challande, Janick Laumonier, Hélène Moingeon, Christian Ollivon, Laurent Philippon, Philippe Szeger and Jean-Christophe Vergez for their technical support to this work.

References

[1] P. Sijtsma, Experimental techniques for identification and characterisation of noise sources, Advances in Aeroacoustics and Applications, VKI Lecture Series 5.

[2] C. S. Allen, W. K. Blake, R. P. Dougherty, D. Lynch, P. T. Soderman, J. R. Underbrink, T. J. Mueller, Aeroacoustic measurements, Springer Science & Business Media, 2013.

[3] P. Sijtsma, Clean based on spatial source coherence, Int. J. Aeroacoustics 6 (4) (2007) 357–374.

[4] T. F. Brooks, W. M. Humphreys, A deconvolution approach for the mapping of acoustic sources (DAMAS) determined from phased microphone arrays, J. Sound Vib. 294 (4) (2006) 856–879.

[5] T. Suzuki, L1 generalized inverse beam-forming algorithm resolving coherent/incoherent, distributed and multipole sources, J. Sound Vib. 330 (24) (2011) 5835–5851.

[6] Q. Leclere, A. Pereira, C. Bailly, J. Antoni, C. Picard, A unified formalism for acoustic imaging based on microphone array measurements, Int. J. Aeroacoustics 16 (4-5) (2017) 431–456.

[7] G. Battista, P. Chiariotti, M. Martarelli, P. Castellini, Inverse methods in aeroacoustic three-dimensional volumetric noise source localization and quantification, J. Sound Vib. 473 (1) (2020) 115208.

[8] S. Moreau, M. Roger, Back-scattering correction and further extensions of Amiet's trailing-edge noise model. Part II: Application, J. Sound Vib. 323 (2009) 397–425.

[9] R. Amiet, Refraction of sound by a shear layer, J. Sound Vib. 58 (4) (1978) 467–482.

[10] J. Fischer, C. Doolan, Beamforming in a reverberant environment using numerical and experimental steering vector formulations, Mech. Syst. Signal Process. 91 (2017) 10–22.

[11] S. Bousabaa, J. Bulté, D. Mincu, R. Marchiano, F. Ollivier, Sparse green's functions estimation using orthogonal matching pursuit: Application to aeroacoustic beamforming, AIAA J. 56 (2018) 2252–2270.

[12] M. Lehmann, D. Ernst, M. Schneider, C. Spehr, M. Lummer, Beamforming for measurements under disturbed propagation conditions using numerically calculated Green's functions, J. Sound Vib. 520 (2022) 116638.

[13] M. Kaltenbacher, B. Kaltenbacher, S. Gombots, Inverse scheme for acoustic source localization using microphone measurements and finite element simulations, Acta Acust. United Acust. 104 (2018) 647–656.

[14] M. Fink, Time-reversed acoustics, Scientific American 281 (5) (1999) 91–97.

[15] M. Fink, C. Prada, Acoustic time-reversal mirrors, Inverse problems 17 (1).

[16] P. Roux, M. Fink, Experimental evidence in acoustics of the violation of time-reversal invariance induced by vorticity, EPL (Europhysics Letters) 32 (1) (1995) 25.

[17] A. Deneuve, P. Druault, R. Marchiano, P. Sagaut, A coupled time-reversal/complex differentiation method for aeroacoustic sensitivity analysis: towards a source detection procedure, J. Fluid Mech. 642 (2010) 181.

[18] P. Druault, R. Marchiano, P. Sagaut, Localization of aeroacoustic sound sources in viscous flows by a time reversal method, J. Sound Vib. 332 (15) (2013) 3655–3669.

[19] I. Rakotoarisoa, D. Marx, C. Prax, V. Valeau, Array processing for the localisation of noise sources in hot flows, Mech. Syst. Signal Process. 116 (2019) 160–172.

[20] I. Rakotoarisoa, Evaluation de technique temporelles pour l'antennerie appliqué à l'imagerie acoustique en écoulement, Ph.D. thesis, Université de Poitiers (2015).

[21] S. M. Candel, Numerical solution of conservation equations arising in linear wave theory: application to aeroacoustics, J. Fluid Mech. 83 (3) (1977) 465–493.

[22] T. Padois, C. Prax, V. Valeau, D. Marx, Experimental localization of an acoustic sound source in a wind-tunnel flow by using a numerical time-reversal technique, J. Acoust. Soc. Am. 132 (4) (2012) 2397–2407.

[23] C. Bailly, D. Juvé, Numerical solution of acoustic propagation problems using linearized Euler equations, AIAA J. 38 (1) (2000) 22–29.

[24] I. Rakotoarisoa, J. Fischer, V. Valeau, D. Marx, C. Prax, L.-E. Brizzi, Time-domain delay-and-sum beamforming for time-reversal detection of intermittent acoustic sources in flows, J. Acoust. Soc. Am. 136 (5) (2014) 2675–2686.

[25] L. Wei, M. Li, D. Yang, F. Niu, W. Zeng, Reconstruction of sound source signal by analytical passive TR in the environment with airflow, J. Sound Vib. 392 (2017) 77–90.

[26] A. Mimani, Z. Prime, D. Moreau, C. Doolan, An experimental application of aeroacoustic time-reversal to the aeolian tone, J. Acoust. Soc. Am. 139 (2) (2016) 740–763.

[27] A. Mimani, D. J. Moreau, Z. Prime, D. C. J., Enhanced focal-resolution of dipole sources using aeroacoustic time-reversal in a wind tunnel, Mech. Syst. Signal Process. 72–73 (2016) 925–937.

[28] A. Mimani, A point-like enhanced resolution of experimental aeolian tone using an iterative point-time-reversal-sponge-layer damping technique, Mech. Syst. Signal Process. 151 (2021) 107411.

[29] A. Mimani, J. Fischer, D. Moreau, C. Doolan, A comparison of time-reversal and cross-spectral beamforming for localizing experimental rod-airfoil interaction noise sources, Mech. Syst. Signal Process. 111 (2018) 456–491.

[30] C. Vanwynsberghe, R. Marchiano, F. Ollivier, P. Challande, H. Moingeon, J. Marchal, Design and implementation of a multi-octave-band audio camera for realtime diagnosis, Appl. Acoust. 89 (2015) 281–287.

[31] Y. Zhou, F. Ollivier, P. Challande, R. Marchiano, V. Valeau, D. Marx, C. Prax, Design and use of a three-dimensional array of MEMS microphones for aeroacoustic measurements in wind-tunnels, in: 8th Berlin Beamforming Conference (BeBeC), 2020.

[32] C. Vanwynsberghe, P. Challande, J. Marchal, R. Marchiano, F. Ollivier, A robust and passive method for geometric calibration of large arrays, J. Acoust. Soc. Am. 139 (3) (2016) 1252–1263.

[33] C. K. Tam, J. C. Webb, Dispersion-relation-preserving finite difference schemes for computational acoustics, J. Comput. Phys. 107 (2) (1993) 262–281.

[34] M. Fink, D. Cassereau, A. Derode, C. Prada, P. Roux, M. Tanter, J.-L. Thomas, F. Wu, Time-reversed acoustics, Rep. Prog. Phys. 63 (2000) 1933–1995.

[35] J. S. Hesthaven, T. Warburton, Nodal discontinuous Galerkin methods: algorithms, analysis, and applications, Springer Science & Business Media, 2007.

[36] A. Luca, R. Marchiano, J.-C. Chassaing, Numerical Simulation of Transit-Time Ultrasonic Flowmeters by a Direct Approach, IEEE Trans. Ultrason. Ferroelectr. Freq. Control 63 (6) (2016) 886–897.

[37] D. C. Wilcox, et al., Turbulence modeling for CFD, Vol. 2, DCW industries La Canada, CA, 1998.

[38] F. R. Menter, Two-equation eddy-viscosity turbulence models for engineering applications, AIAA J. 32 (8) (1994) 1598–1605.

[39] Y. Zhou, V. Valeau, J. Marchal, F. Ollivier, R. Marchiano, Three-dimensional identification of flow-induced noise sources with a tunnel-shaped array of MEMS microphones, J. Sound Vib. 482 (2020) 115459.

[40] S. Candel, A. Guedel, A. Julienne, Résultats préliminaires sur la diffusion d'une onde acoustique par écoulement turbulent, Le Journal de Physique Colloques 37 (C1) (1976) C1–153.

[41] T. Padois, Localisation de source acoustique en soufflerie anéchoïque par deux techniques d'antennerie: formation de voies et retournement temporel numérique, Ph.D. thesis, Université de Poitiers (2011).

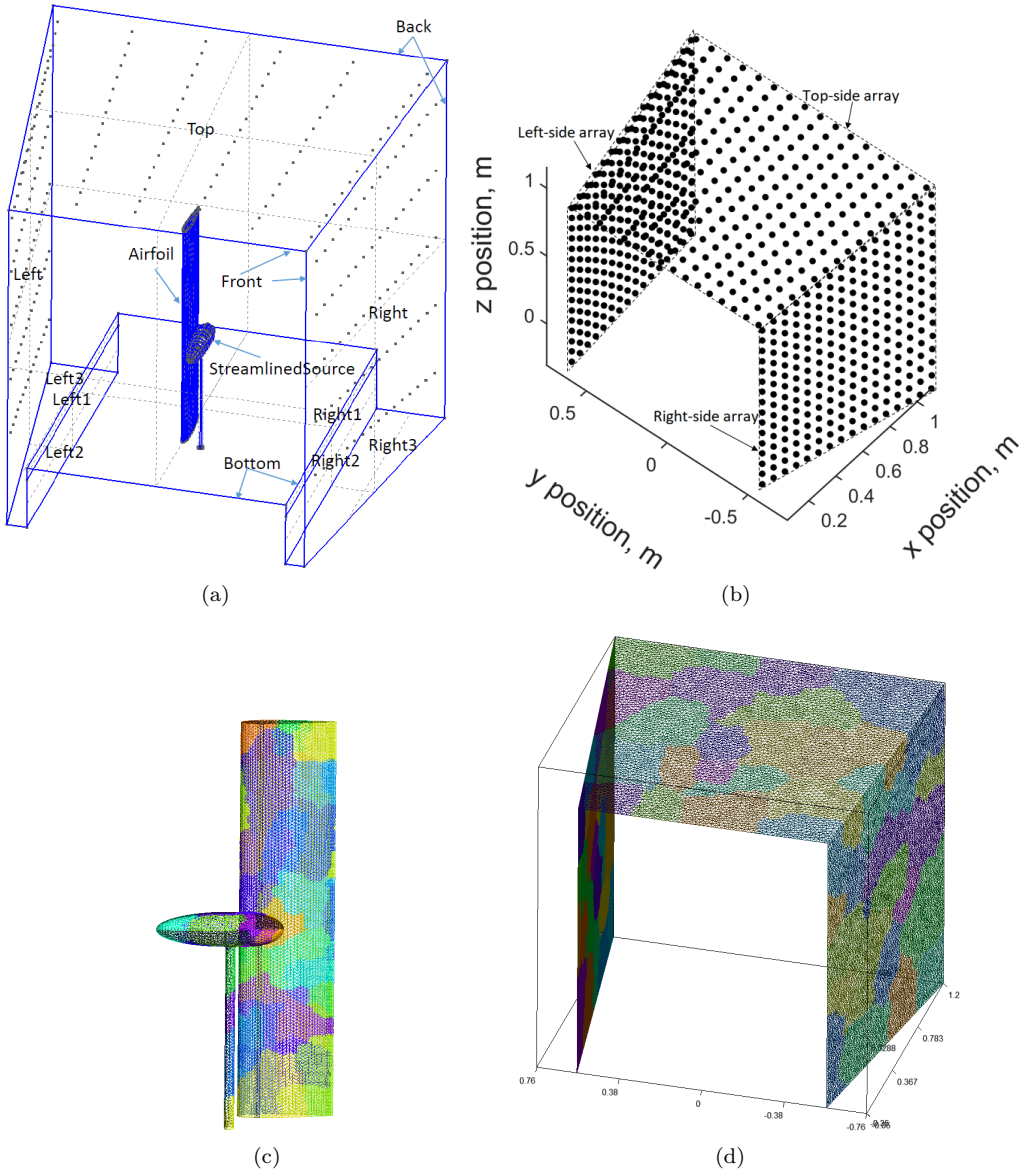

Figure 6: 3D acoustic mesh of a NACA 0012 airfoil at an angle of attack $\alpha = 0°$ and of the streamlined acoustic source, using GMSH. (a) The domain of the 3D acoustic mesh with the positions of 256 microphones indicated by the black points on the three patches 'Left', 'Top' and 'Right' of the domain; (b) arrangement of microphones for a 3D array with 768 microphones; (c) the triangular mesh elements on the patches of 'Airfoil' and 'StreamlinedSource'. The mesh elements with different colors in (c) correspond to different partitions; (d) the triangular mesh elements on the patches of 'Left', 'Top' and 'Right'. The different colors in figures (c) and (d) are due to the mesh partitions.

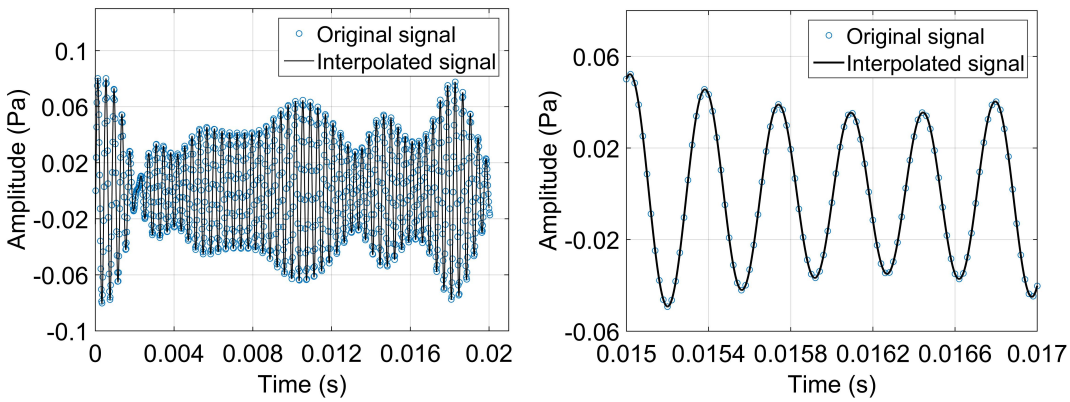

(a) (b)

Figure 7: (a) Original signal of the channel 545 and the interpolated signal; (b) a zoom of (a).

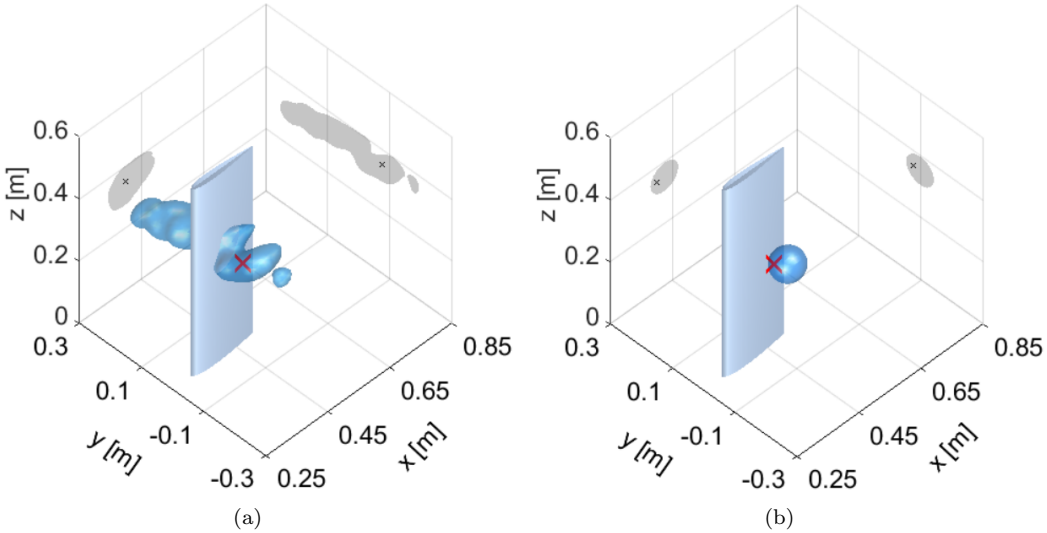

(a) (b)

Figure 8: Sound maps for the synthetic noise source diffracted by a NACA 0012 airfoil at an angle of attack $\alpha = 0°$, at a third-octave bands of nominal midband frequency 2.5 kHz. The shadows and the red symbols 'x' correspond respectively to the projection of the 3D sound source imaging and the noise source position. (a): 3D beamforming with a maximum value of 56.2 dB on the sound map; (b): CLEAN-SC technique with a maximum value of 56.1 dB on the sound map. The 3D isosurface in each sound map is plotted at 9 dB below the maximum value of the sound map.

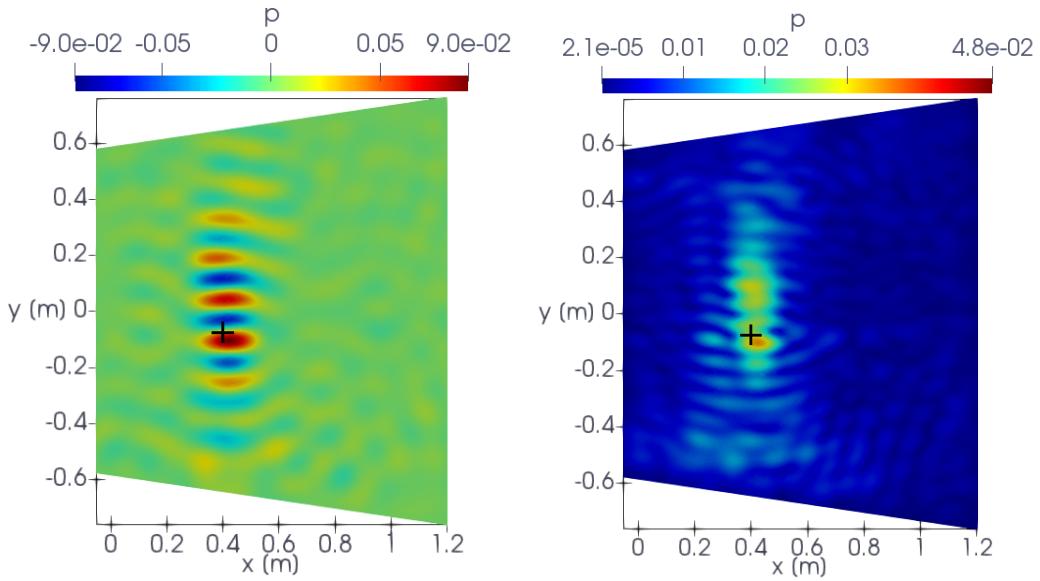

(a) (b)

Figure 9: Results of the 3D TR for the synthetic noise source emitted by the streamlined body shown in the third-octave band [2245; 2828] Hz. 256 channels of acoustic data are used. The solid boundaries of the objects are not considered for the numerical simulation. (a) Snapshot of the pressure field in a planar cross section XY at $z = 0.35$ m; (b) RMS of the pressure field from 0.005 s to 0.015 s in the same plane.

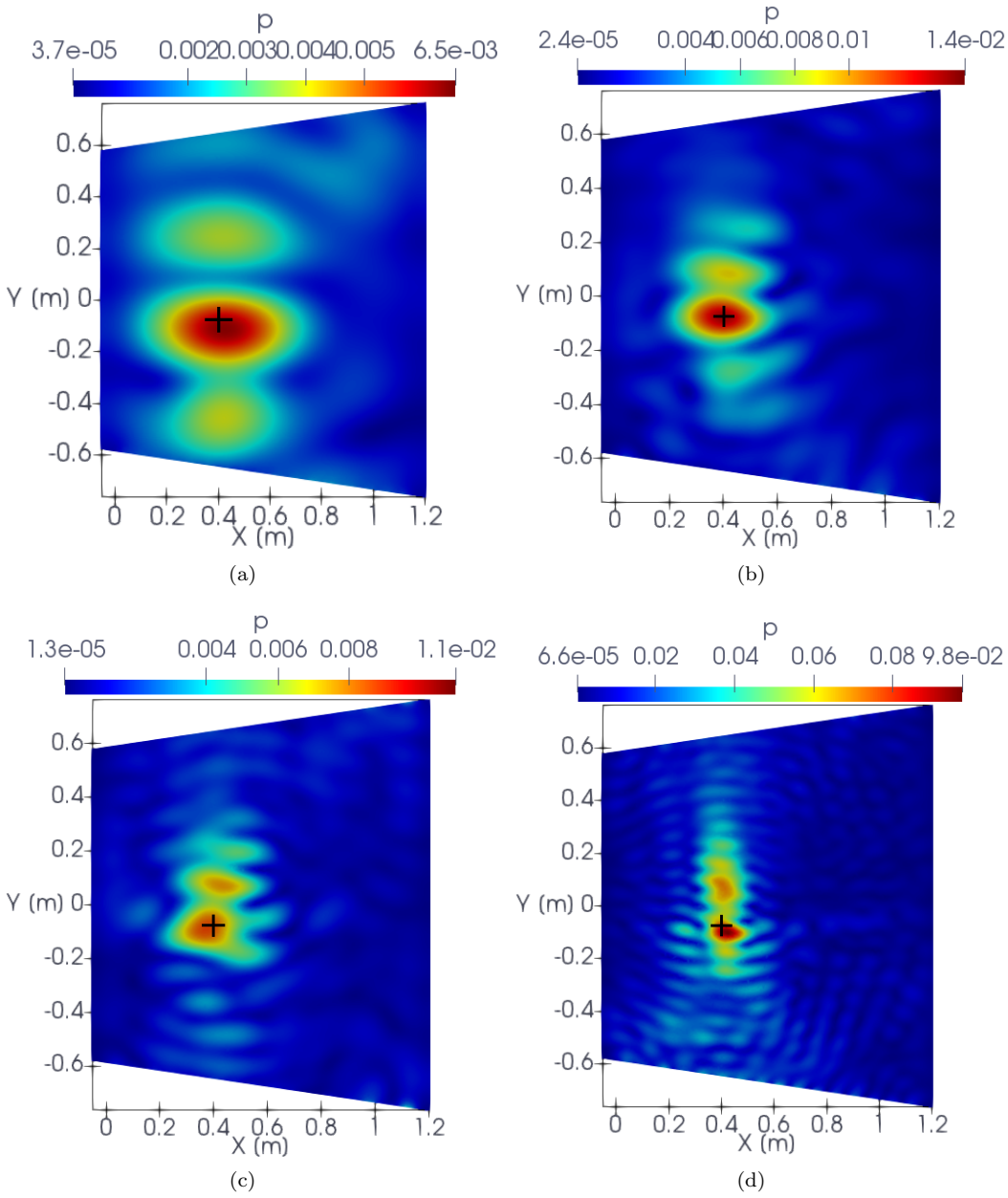

Figure 10: Results of the 3D TR for the synthetic noise source emitted by the streamlined body shown in a planar cross section XY at $z = 0.35$ m. 768 channels of acoustic data are used. The solid boundaries of the objects are not considered during the numerical simulation. RMS of the pressure field from 0.005 s to 0.015 s in the third-octave band (a) [561; 707] Hz; (b) [1122; 1414] Hz; (c) [1414; 1782] Hz; (d) [2245; 2828] Hz.

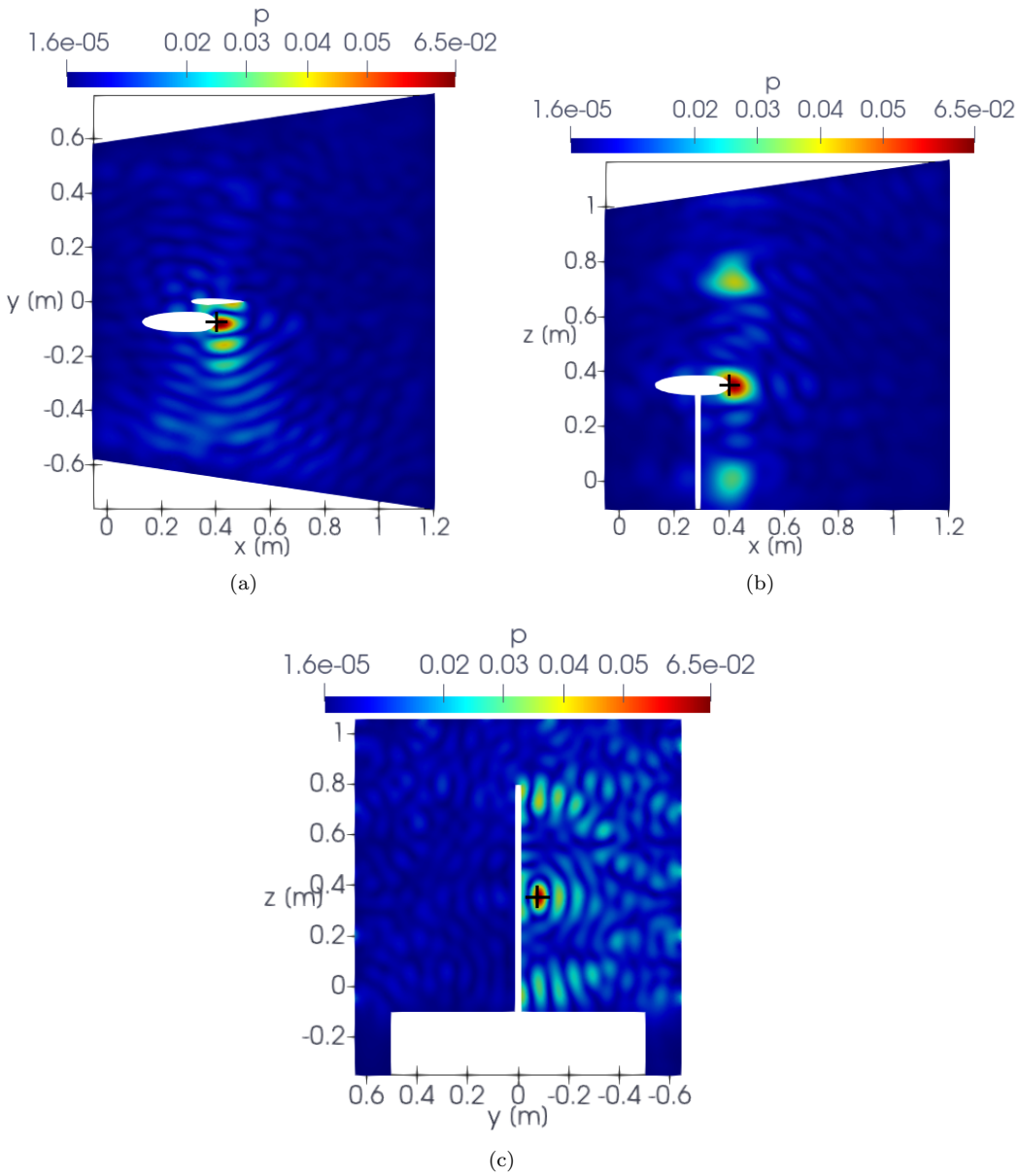

(a) (b) (c)

Figure 11: Results of the 3D TR for the synthetic noise source emitted by the streamlined body shown in different cross sections in the third-octave band [2245; 2828] Hz. RMS of the pressure field from 0.005 s to 0.015 s with 256 channels of acoustic data (a) in a planar cross section XY at $z = 0.35$ m; (b) in a planar cross section XZ at $y = -0.075$ m; (c) in a planar cross section YZ at $x = 0.402$ m.

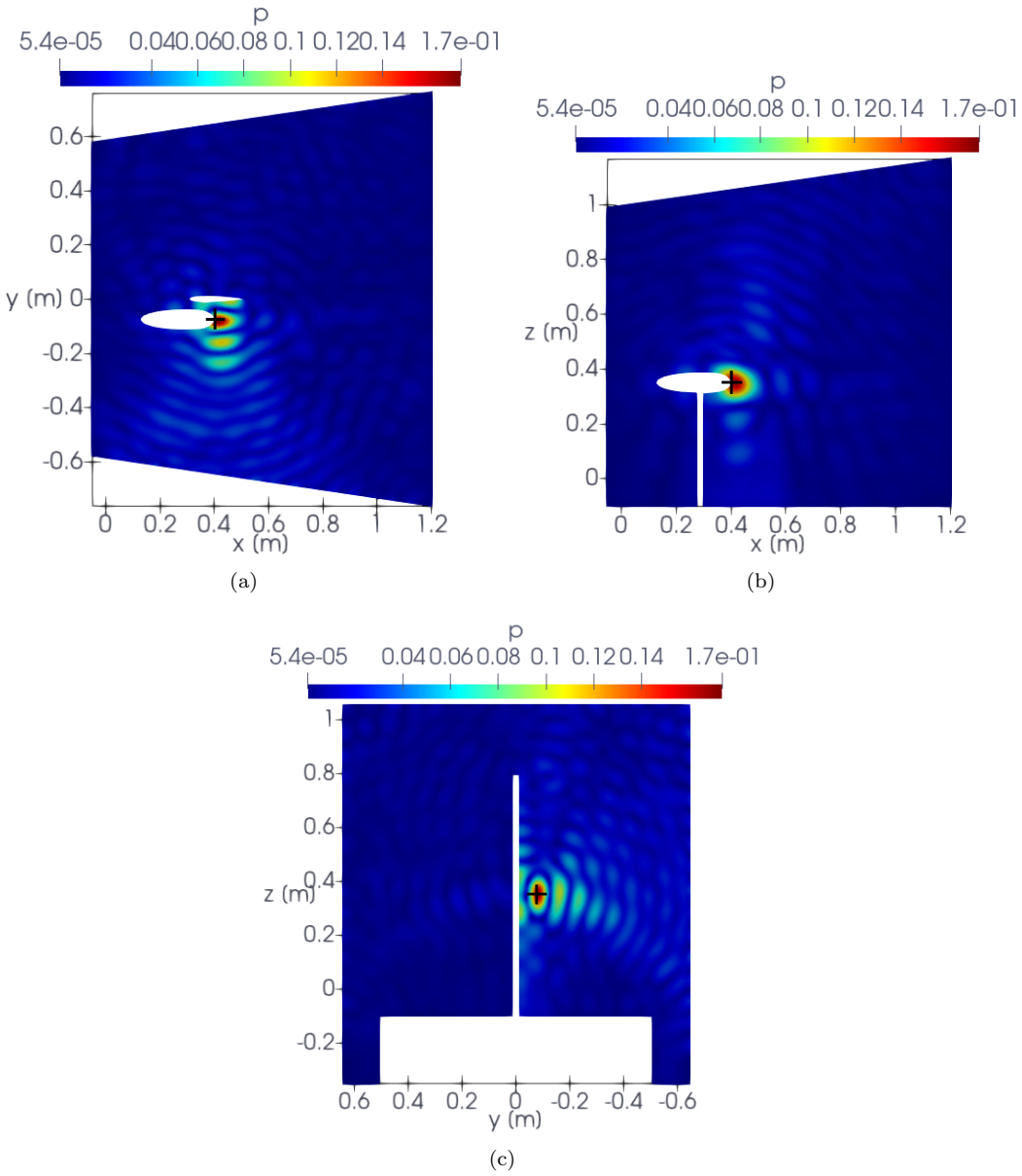

(a) (b) (c)

Figure 12: Results of the 3D TR for the synthetic noise source emitted by the streamlined body shown in different cross sections in the third-octave band [2245; 2828] Hz. RMS of the pressure field from 0.005 s to 0.015 s with 768 channels of acoustic data (a) in a planar cross section XY at $z = 0.35$ m; (b) in a planar cross section XZ at $y = -0.075$ m; (c) in a planar cross section YZ at $x = 0.402$ m.

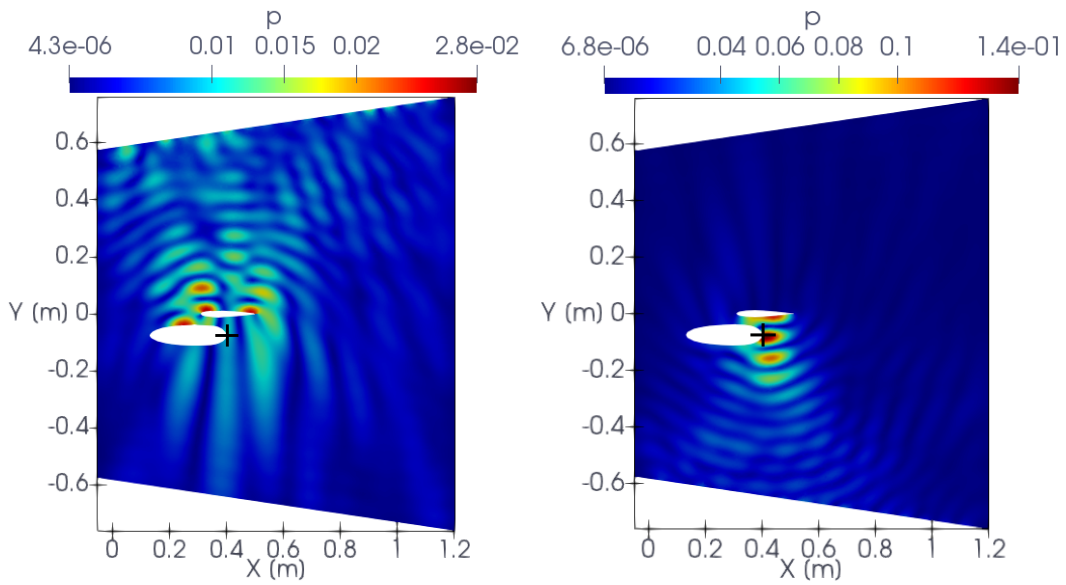

(a) (b)

Figure 13: Results of the 3D TR for the synthetic noise source emitted by the streamlined body shown in the third-octave band [2245; 2828] Hz. RMS of the pressure field from 0.005 s to 0.015 s in a planar cross section XY at $z = 0.35$ m with (a) 256 channels of acoustic data using the left-side array; (b) 256 channels of acoustic data using the right-side array.

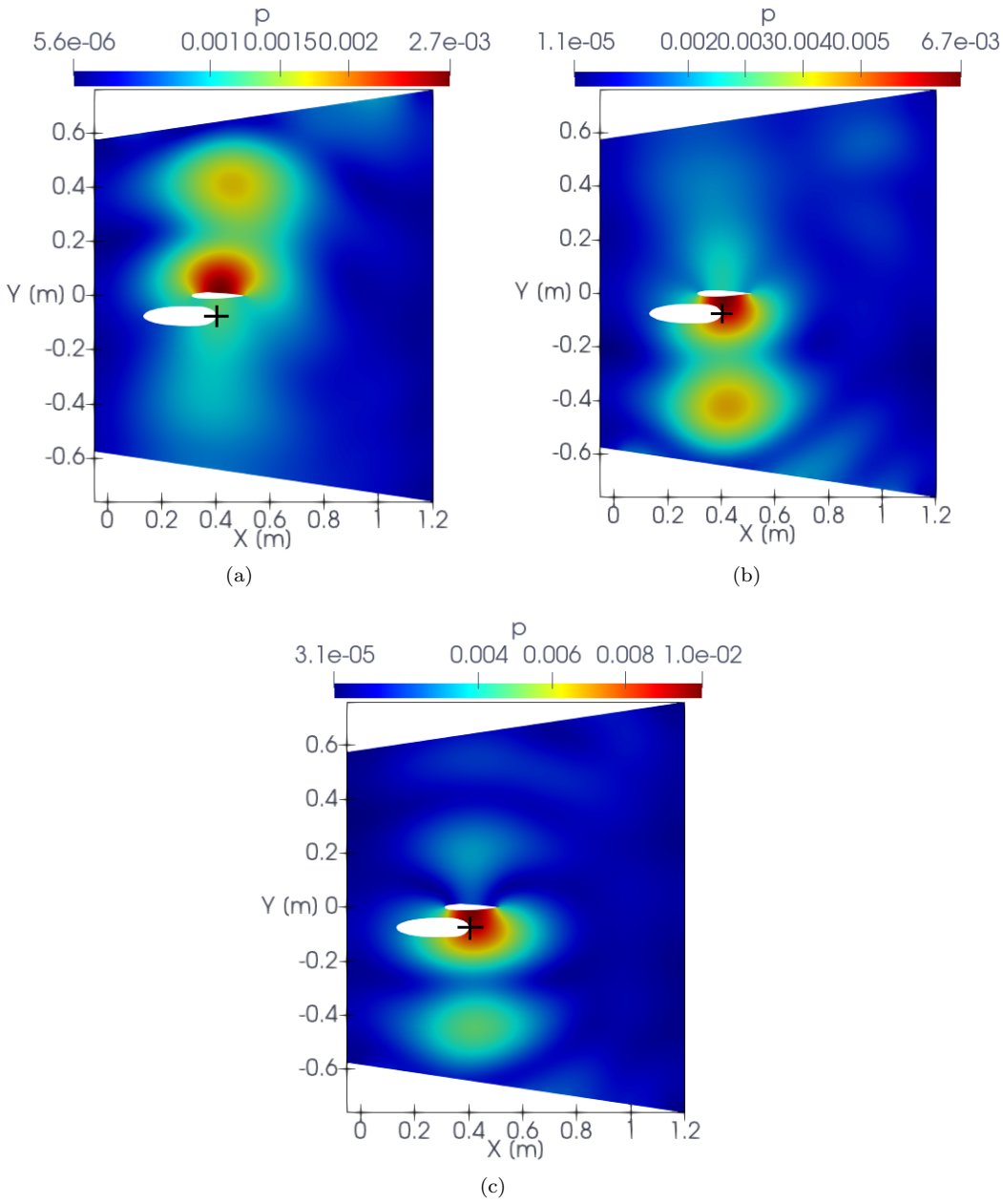

Figure 14: Results of the 3D TR for the synthetic noise source emitted by the streamlined body shown in the third-octave band [561; 707] Hz. RMS of the pressure field from 0.005 s to 0.015 s in a planar cross section XY at $z = 0.35$ m with (a) 256 channels of acoustic data using the left-side array; (b) 256 channels of acoustic data using the right-side array; (c) 768 channels of acoustic data of the entire array. The source known position is indicated with a cross.

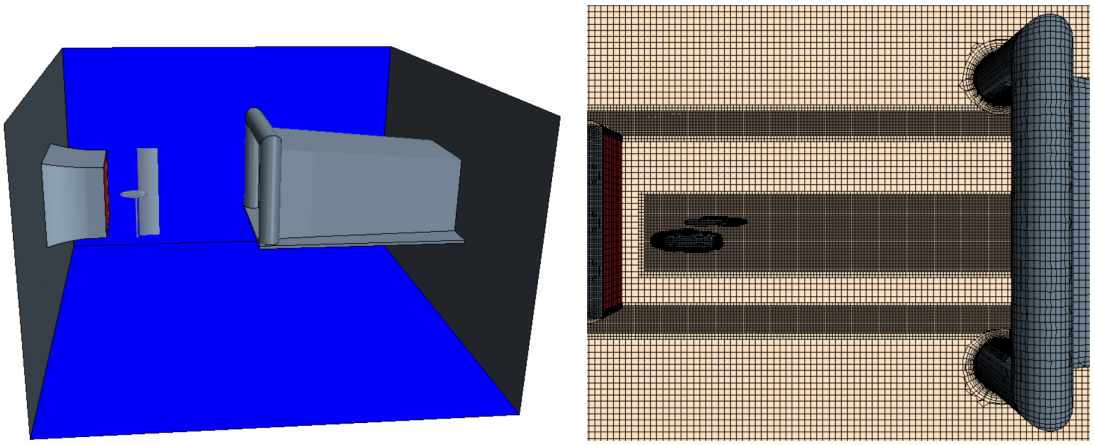

(a) (b)

Figure 15: (a) The computational domain for RANS simulation. The objects are the nozzle, the streamlined acoustic source, the airfoil and the collector from left to right; (b) mesh of RANS simulation in a planar cross section XY at $z = 0.35$.

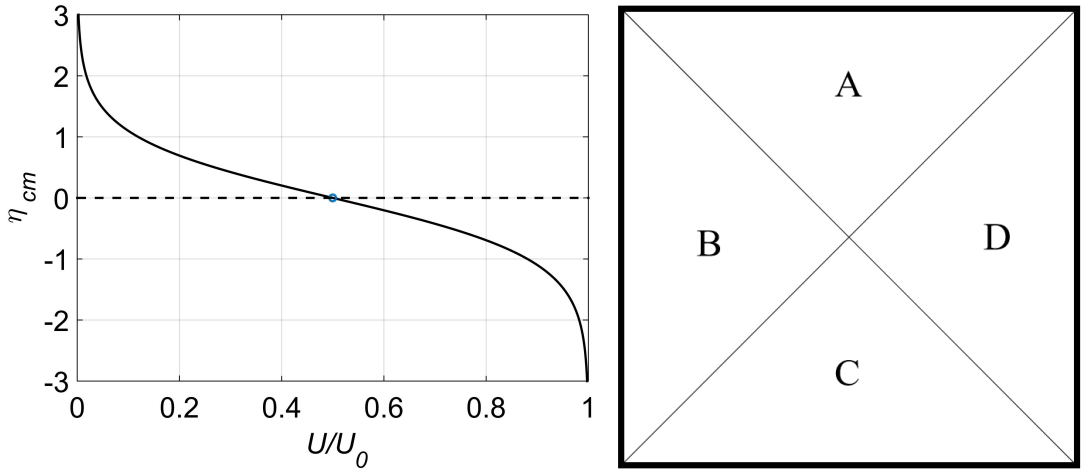

(a) (b)

Figure 16: (a) Analytical velocity profile (given by Eq. (6)); (b) the four parts of the inflow patch for setting velocity at the nozzle exit.

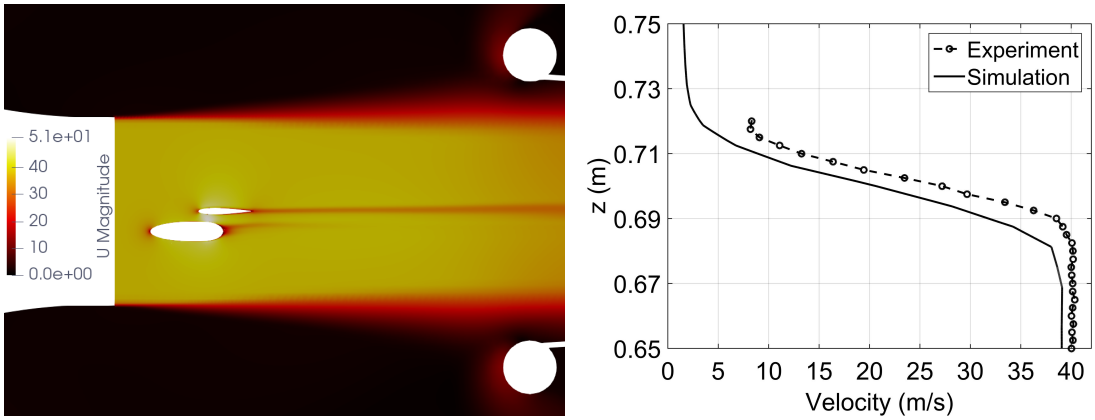

(a) (b)

Figure 17: (a) The mean flow velocity of the wind-tunnel flow in a planar cross section XY at $z = 0.35$ m; (b) comparison between the numerical result and experimental result for a velocity profile along the $z-$direction for a shear layer.

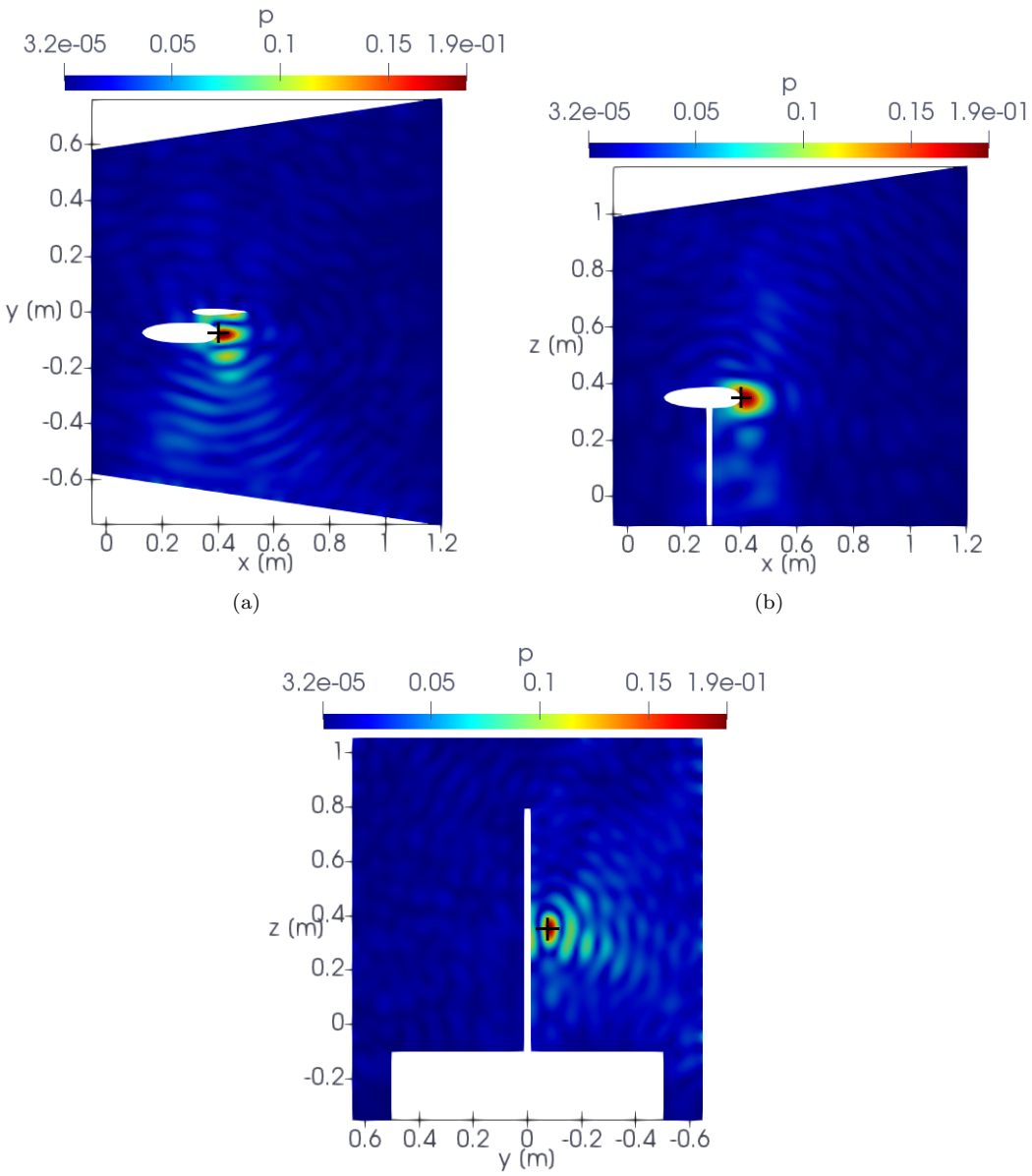

Figure 18: Results of the 3D TR for the synthetic noise source emitted by the streamlined body shown in different cross sections in the third-octave band [2245; 2828] Hz. The incoming velocity is 39.2 m/s. 768 channels of acoustic data are used. RMS of the pressure field from 0.005 s to 0.01 s (a) in a planar cross section XY at $z = 0.35$ m; (b) in a planar cross section XZ at $y = -0.075$ m; (c) in a planar cross section YZ at $x = 0.402$ m.